

Article

Parabola-Like Gold Nanobowtie on Sapphire Substrate as Nano-Cavity

Wenbing Li ¹, Zhuo Yang ^{1,2}, Jiali Zhang ^{1,2}, Xin Tong ^{1,2}, Yuheng Zhang ^{1,2}, Bo Liu ^{1,2,*} and Chao Ping Chen ^{3,*} 

¹ Shanghai Industrial μ Technology Research Institute, Shanghai 201800, China; quentin.li@sitrigroup.com (W.L.); yz98@shu.edu.cn (Z.Y.); jallyzhang@shu.edu.cn (J.Z.); tongxin@shu.edu.cn (X.T.); 1170832697@shu.edu.cn (Y.Z.)

² School of Microelectronics, Shanghai University, Shanghai 201800, China

³ Smart Display Lab, Department of Electronic Engineering, Shanghai Jiao Tong University, Shanghai 200240, China

* Correspondence: steven.liu@sitrigroup.com (B.L.); ccp@sjtu.edu.cn (C.P.C.)

Abstract: Plasmonic metallic nanostructures have attracted much interest for their ability to manipulate light on a subwavelength scale and for their related applications in various fields. In this work, a parabola-like gold nanobowtie (PGNB) on a sapphire substrate was designed as a nano-cavity for confining light waves in a nanoscale gap region. The near-field optical properties of the innovative PGNB structure were studied comprehensively, taking advantage of the time-resolved field calculation based on a finite-difference time-domain algorithm (FDTD). The calculation result showed that the resonance wavelength of the nano-cavity was quite sensitive to the geometry of the PGNB. The values that related to the scattering and absorption properties of the PGNB, such as the scattering cross section, absorption cross section, extinction cross section, scattering ratio, and also the absorption ratio, were strongly dependent on the geometrical parameters which affected the surface area of the nanobowtie. Increased sharpness of the gold tips on the parabola-like nano-wings benefited the concentration of high-density charges with opposite electric properties in the narrow gold tips with limited volume, thus, resulting in a highly enhanced electric field in the nano-cavity under illumination of the light wave. Reduction of the gap size between the two gold nano-tips, namely, the size of the nano-cavity, decreased the distance that the electric potential produced by the highly concentrated charges on the surface of each gold nano-tip had to jump across, therefore, causing a significantly enhanced field in the nano-cavity. Further, alignment of the linearly polarized electric field of the incident light wave with the symmetric axis of the PGNB efficiently enabled the free electrons in the PGNB to concentrate on the surface of the sharp gold tips with a high density, thus, strongly improving the field across the nano-cavity. The research provides a new insight for future design, nanofabrication, and characterization of PGNBs for applications in devices that relate to enhancing photons emission, improving efficiency for energy harvesting, and improving sensitivity for infrared detection.

Keywords: plasmonic; parabola-like gold nanobowtie (PGNB); nano-cavity; finite-difference time-domain (FDTD); field enhancement; charge distribution



Citation: Li, W.; Yang, Z.; Zhang, J.; Tong, X.; Zhang, Y.; Liu, B.; Chen, C.P. Parabola-Like Gold Nanobowtie on Sapphire Substrate as Nano-Cavity. *Photonics* **2022**, *9*, 193. <https://doi.org/10.3390/photonics9030193>

Received: 20 February 2022

Accepted: 15 March 2022

Published: 17 March 2022

Publisher's Note: MDPI stays neutral with regard to jurisdictional claims in published maps and institutional affiliations.



Copyright: © 2022 by the authors. Licensee MDPI, Basel, Switzerland. This article is an open access article distributed under the terms and conditions of the Creative Commons Attribution (CC BY) license (<https://creativecommons.org/licenses/by/4.0/>).

1. Introduction

Plasmonic metallic nano-antennas, such as metallic nanoparticles over a metal thin film with ultrathin nanogaps [1–3] or closely spaced nanoparticles with tiny nanogaps [4,5], can confine light waves at subwavelength volumes in the nano-cavities formed in the gaps, while the electric field of the incident photons interacts with the free electrons that are oscillating in the metallic nanostructure. At the resonance frequency of the nano-cavity formed in the nano-antenna, a highly enhanced localised field is trapped by the gap mode. It leads to wide applications in surface-enhanced Raman microscopy [6–8], enhancement

of light emission efficiency in InGaN/GaN-based light-emitting diodes [9], improving the spontaneous emission of quantum dot LEDs [10], enhancing fluorescence emission for biotechnology [11], harvesting solar energy for photovoltaic cells [12], and high-sensitivity photodetection in infrared range [13–15].

To understand the physics of plasmonic nano-antennas, particularly nanobowtie antennas, extensive research has focused on using advanced nanofabrication techniques and various optical characterization methods to study the optics of the metallic nano-antennas [16–22]. For instance, electron beam lithography and focused ion beam miller, with the advantage of being able to overcome the diffraction limit of deep-ultraviolet photolithography when determining a fine nanostructure, were used to fabricate nanobowties with sub-10-nm gaps [16,17,23], and also self-assembled nanosphere lithography was often applied as an economic technique to fabricate nanobowties with a hexagonal arrangement [18]. A near-field scanning optical microscope (NSOM), with a polarization-controlled laser source and a sharp tip that can sense the optical intensity close to a target nanostructure, was used as an analytical tool by Rui Guo et al. to map the optical field in the micron-scale region at different heights around an aluminum nanobowtie aperture [20]. The electron energy loss spectrum (EELS) was used by V. Krapek et al. to image the optical mode of a nanobowtie at various resonance frequencies and to study the relationship between the geometrical parameters and the localized surface plasmonic resonance peak [19].

Currently, with the fast improvement of high-performance computer technology and the development of various numerical algorithms for solving the Maxwell's equations aimed at nanophotonic research, the study of the optics of nano-antennas based on the finite element method (FEM) [20,24,25], finite-difference time-domain method (FDTD) [26–28], discrete-dipole approximation (DDA) [4,29], boundary element methods (BEM) [29,30], and the nanocircuits model [31–36] has attracted extensive interest. Taking advantage of the FEM algorithm to find the eigen-frequency (value) solution, Weihua Wang et al. studied the plasmonic eigen-modes of a graphene nanobowtie based on a classical, electromagnetic model and a quantum-confined model through a 2D FEM approach [24]. Guanqing Du et al. studied the optical trapping potential of Au–Au homogeneous and Au–Ag heterogeneous triangle nanobowties based on two-dimensional FEM methods and realized the tunability of the trapping potential symmetry for an Au–Ag heterogeneous triangle nanobowtie through variation of incident laser electric fields [25]. Bin Wang et al. investigated the geometry influence of the localized plasmonic resonance of an aluminum-based bowtie antenna array based on the FDTD method and used the designed nanostructure as an index sensor for biology sensing [26]. Martin Hrtoň et al. comparatively evaluated the optical spectroscopy and optical trapping properties of Au nano-antennas, including nanobowties and nanodiabolo and their corresponding inverted nanostructures, based on the FDTD method and revealed the electromagnetic hotspot feature following Babinet's principle [28]. As an analogy for the radio frequency electromagnetic waves interacting with LCR resonance circuits or the emission of RF antennas, the subwavelength nanoscale metamaterial under illumination of light wave was considered as optical nanocircuits where the nano-geometry with different permittivity can be seen as nano-inductors, nano-capacitors, and nano-resistors [33,34]. As an analytical model that is unnecessary to get the complex numerical algorithm involved in the solving of Maxwell's equations, the nanocircuits model has also attracted much attention [31,32]. In addition, the magnetic-optical properties of a plasmonic nano-cavity with a metal-dielectric-metal waveguide-coupled flow resonant mode was studied theoretically by Ji-Song Pae et al., and the resulting potential applications for high-speed on-chip memory were figured out [37]. In the material model, magnetization was involved in the permittivity tensor elements, together with a magneto-optical susceptibility as a coefficient [37]. With the advantage of processing 2D material as graphene by an analytical material model, M. Dudek et al. studied a Fabry–Pérot micro-cavity based on a graphene-based, hyperbolic metamaterials platform by the FDTD method, demonstrating the polarization-dependent tunability of resonant

frequencies in the mid-infrared range with modulating thickness of dielectric layers, and therefore reporting the potential application as an edge filter [38].

In this work, a single PGNB sitting on a sapphire substrate was simulated under illumination of a broad-wavelength incident light wave with a specified polarization angle, taking advantage of the time-resolved field simulation of the FDTD algorithm. Thus, the frequency-spectra-dependent field in a three-dimensional space was obtained from the FFT of the time-dependent field in a single run of time evolution. In a comprehensive investigation of the geometry influence, the optical spectra properties, such as the scattering cross section, absorption cross section, extinction cross section, and field enhancement factor, were calculated with various thicknesses, wing widths, and gap sizes of the PGNB across a broad wavelength range from 300 nm to 2 μm . The result showed that the PGNB on the sapphire substrate worked like an optical nano-cavity and that the resonance peak shifted with variation of the geometrical parameters. The optical electric field over the simulation region and the charges distribution on the surface of the PGNB indicated that the resonance wavelength strongly responded to the oscillation of free electrons confined in the PGNB under illumination of light waves with various frequencies. The scattering and absorption ratio of incident light across the ultraviolet to near-infrared range uncovered the optimized geometry of the PGNB as a scatterer or absorber, which has field applications such as being a SERS substrate for biosensing, a plasmonic absorber for energy harvesting, and a plasmonic nano-heater for biotechnology. The average field enhancement factor over the simulation region and the average field enhancement factor over the gap region disclosed the optimized incident wavelength and bowtie geometry for maximization of the enhanced field. In addition, the simulation result also pointed out the optimized polarization angle of the incident wave to illuminate the PGNB, and the redistribution of charges on the surface of the PGNB under the illumination of electric fields with a specified polarization direction. Our simulation, optimization, and design of the PGNB provides a new insight for future nanofabrication of the device and its application in related fields.

2. Design and Method

The FDTD algorithm takes advantage of the leap-frog, discrete method that separates Ampère's equation and Faraday's equation in a 3-dimensional space with multiple Yee grids in a time evolution, in which the future electric field can be obtained from the previous electric field and current magnetic field, and the future magnetic field can be obtained from the previous magnetic field and current electric field [39]. The optical constants of the materials involved appear in the update coefficients dependent on frequency, and the Courant stability condition that connects the time steps and Yee grids, ensuring the stability of the calculation [39]. The dispersive refractive index values of gold and sapphire used in this simulation were obtained from reference (the refractive index values of gold and sapphire used in this calculation are displayed in Figure S1 of the Supplementary Materials) [40,41]. A Drude model was used to express the dispersion of dielectric function of gold material, with the assumption that the free-electron gas in the metal oscillating against the background of positive nuclei under a harmonic time-dependent field [42]. However, in the case of incident photons above the threshold energy 1.8 eV, it deviated from the experiment data for the inter-band transitions, and we needed to add Lorentzian terms to introduce bounded oscillators [43,44]. For the gold material used in this work, an expression with the following multiple Lorentzian terms fitted with the test data well with the parameters from reference [45]:

$$\varepsilon(\omega) = \varepsilon_{\infty} + \frac{\sigma/\varepsilon_0}{j\omega} + \sum_{p=1}^p \frac{C_p}{\omega^2 + A_p j\omega + B_p} \quad (1)$$

where $\varepsilon(\omega)$ was the permittivity of gold material dependent on angular frequency ω , ε_{∞} was the high-frequency dielectric constant, σ was the conductivity of gold, ε_0 was the vacuum permittivity, and A_p , B_p and C_p were the coefficients for the fitting Drude–Lorentz model. The geometry of the PGNB over a sapphire substrate is presented in Figure 1a. The

selection of sapphire as the substrate for the PGNB was made as it is an economic and commonly used transparent substrate for fabrication of GaN-based LEDs or power devices in the semiconductor industry. The shape of the PGNB was controlled by the thickness of a gold thin film (for fabrication of the gold nanobowtie) deposited on a sapphire substrate by PVD (symbolized as H), the wing width of the edge of the PGNB (symbolized as W), the wing length between the vertex and the edge (symbolized as L), and the size of the gap between the vertex of each parabola (symbolized as Gap), which was shown in Figure 1. The geometrical model was located in a Cartesian coordinate system for the calculation, where the center of the gap was matched with the origin of the Cartesian coordinate system, and the middle line of the PGNB was oriented at the *y*-axis. The forward direction of the *z*-axis was bottom-up-oriented on the sapphire substrate, and the zero point at the *z*-axis was located on the top surface of the sapphire substrate. As a single PGNB above a sapphire substrate, perfectly matched layers (PMLs) were used to enclose the simulation object where the scattered waves would be absorbed [46]. In the free space, the edges of the PMLs were kept more than half a wavelength from the simulation domain to reduce possible reflections from the PMLs. For simplification, the sapphire substrate was assumed to be semi-infinite, that only the interface between the surface of the sapphire and the gold nanostructure (free space) was considered, and the light traveling in the sapphire substrate would disappear when it touched the PMLs truncating the substrate [39]. The edge shape of the nanobowtie was controlled by a parabola equation $y = \left(\frac{4L}{W^2}\right) * x^2 + \frac{Gap}{2}$, and the curvature of the vertex was determined by wing length L and wing width W. For simplification, the wing length L was kept as a constant 100 nm in the calculation, while the wing width and thickness of the nanobowtie and the gap size between the vertex of each parabola were varied in a certain range: 10–100 nm, 5–100 nm, and 0–15 nm, respectively. A linear polarized total-field scattered-field (TFSF) source, consisting of a series of plane waves, was used as the light wave for illumination of the simulation object [47]. The TFSF source was injected vertically onto the surface of the sapphire substrate toward the PGNB with a specified polarization angle in which the zero-polarization angle was oriented at the forward direction of the *x*-axis, and the 90-degree polarization angle was oriented at the forward direction of the *y*-axis. For the linearity of Maxwell’s equation, the total field was separated into the incident field and the scattered field that the area contained; the scatter (total field) and the region around the scatter (scattered field) were separated [47].

Since the simulation region was divided into the total field region that contained the PGNB and the scattered field region with free space outside of the TFSF source, the scattering cross section could be calculated as the ratio between the total scattered power (W) across the scattered field boundary toward the PMLs and the light intensity of the TFSF source (W/m²) injected into the total field region. Meanwhile, the absorption cross section could be computed as the ratio between the absorption power (W) in the total field region and the intensity of the TFSF source (W/m²) injected into the total field region. The expressions for calculating the scattering cross section (σ_{scatt}) and absorption cross section (σ_{abs}), respectively, were displayed as follows [48]:

$$\sigma_{scatt} = \frac{\int \int \vec{E} \times \vec{H} d\vec{S}}{I_s} \tag{2}$$

$$\sigma_{abs} = \frac{\int \int \int \frac{1}{2} \epsilon_0 \omega E^2 \epsilon_r'' dV}{I_s} \tag{3}$$

where \vec{E} and \vec{H} were the frequency and space-dependent electric field vector and magnetic field vector, respectively, I_s was the light intensity of the incident source, ϵ_0 was the vacuum permittivity, ϵ_r'' was the imaginary part of the relative permittivity of material, and ω was the angular frequency of incident source. The sum of the scattering cross section and absorption cross section comprised the extinction cross section. The scattering ratio was defined as the scattered power (the power leaving the PGNB and going across the scattered field boundary toward the PMLs) over the source power injected into the total field region.

Reversely, the absorption ratio was defined as the power absorbed in the total field region over the source power injected into the total field region. For energy conservation, the sum of scattering ratio and absorption ratio was 1 at any wavelength. Replacing the light source intensity in expression (2) and (3) with source power, gave out the scattering ratio and absorption ratio, respectively.

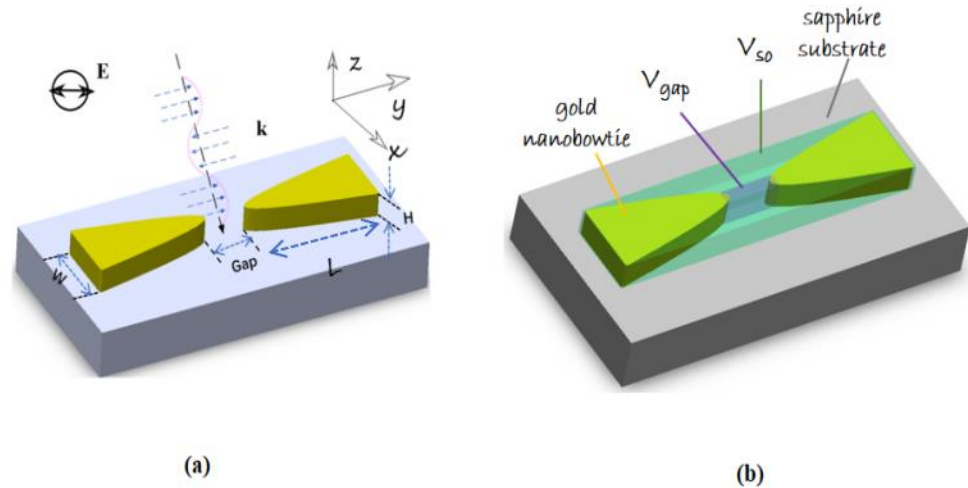


Figure 1. Schematic view of the simulation object. The simulation model consisted of a PGNB made of gold and a sapphire substrate on which the PGNB was standing on. (a) A Cartesian coordinate system was used for the simulation, in which the center of the gap for the nanobowtie was selected to locate the origin of the coordinates, and the axis of the PGNB was matched at the y -axis. The forward direction of the z -axis was bottom-up-oriented and vertical to the surface of the sapphire substrate. A linear, polarized source (a TFSF source consisting of a series of plane waves) with a broad wavelength range was illuminated on the PGNB perpendicularly with a specific polarization angle. (b) The green box shows the integration volume (V_{so}) for calculating the average field enhancement factor over the simulation object and also the volume for calculating the light-wave-absorption power of the PGNB. The violet box shows the integration volume (V_{gap}) for calculating the average field enhancement factor over the gap.

The field enhancement factor in this article was defined as the 2nd order of the ratio between the total field and the incident field [7,8]. As the electric field was a value that was dependent on space and incident wavelength, the field enhancement factor was different at various Yee grid nodes that referred to the 3-dimensional space in the simulation region. Therefore, the average enhancement factor over the simulation object was defined as the ratio between the volume integral of the enhancement factor covered the simulation object region over the volume of the simulation object region in this article (Figure 1b), which was expressed in expression (4):

$$EF = \frac{\int \int \int_0^{V_{so}} (E(x, y, z, f) / E_0(x, y, z, f))^2 dx dy dz}{V_{so}} \tag{4}$$

where V_{so} was the volume of the simulation object region, $E(x, y, z, f)$ was the total electric field value dependent on space and frequency, and $E_0(x, y, z, f)$ was the incident electric field value dependent on space and frequency. In order to characterize the field enhancement factor at the gap of the PGNB, the average field enhancement factor over the gap region was defined (symbolized as gap EF). The volume of the gap region was defined as:

$$V_{gap} = 2\Delta x * (Gap + 2\Delta y) * H \tag{5}$$

where Gap was the size between the vertex of each parabola, H was the height of the PGNB, Δx was the Yee grid size at the x -axis, and Δy was the Yee grid size at the y -axis. Thus, a cubic region with the height of the gold nanobowtie, a length as the sum of the gap between

the vertex of each parabola-like gold nanoparticle and an extension of one Yee grid to each parabola-like gold nanoparticle, and a width with two Yee grids wide across the y -axis were determined for the calculation of the average enhancement factor in the gap region of the PGNB.

Therefore, the average field enhancement factor over the gap was expressed as:

$$EF = \frac{\int \int \int_0^{V_{gap}} (E(x, y, z, f) / E_0(x, y, z, f))^2 dx dy dz}{V_{gap}} \quad (6)$$

where V_{gap} was the volume of the gap region of the PGNB, $E(x, y, z, f)$ was the total field dependent on space and frequency, and $E_0(x, y, z, f)$ was the incident field dependent on space and frequency. The charge density in the PGNB was redistributed, responding to the electric field variation in the simulation region. It was determined by the divergence of the electric field, and it can be given by Gauss's equation [42]:

$$\rho = \epsilon \nabla \cdot \vec{E} \quad (7)$$

where \vec{E} was the electric field, and ϵ was the permittivity of the material.

3. Results and Discussion

3.1. Scattering and Absorption of the PGNB Dependent on Geometry

The simulation result of the PGNB is displayed in Figures 2–7. The scattering cross section, absorption cross section, and extinction cross section values were calculated following expression (2) and (3) under the vertical illumination of a TFSF source, covering the wavelength range from 300 nm to 2 μ m and the electric field polarized at the y -axis (Figure 2). The results of the scattering cross section, absorption cross section, and extinction cross section dependent on the wing width of the PGNB and incident wavelength with a constant wing length of 100 nm, a constant gold thickness of 50 nm, and a gap size of 3 nm were presented in Figure 2a–c. By broadening the wing width W from 10 nm to 100 nm or, in other words, reducing the curvature of the parabola vertex, the resonance peak of all three cross sections showed a blue shift from a near-infrared wavelength above 1.2 μ m to 885 nm with variation of the area for all three cross sections. The scattering cross section value sharply climbed from $9.668 \times 10^3 \text{ nm}^2$ to $8.287 \times 10^4 \text{ nm}^2$ with the broadening of the wing width because the increased surface area of the PGNB was accompanied by a resonance shift from 1272 nm to 885 nm. Reversely, the absorption cross section value showed a slight decrease from $3.805 \times 10^4 \text{ nm}^2$ to $2.818 \times 10^4 \text{ nm}^2$ with the broadening of the wing width, blue-shifting the resonance wavelength from 1227 nm to 885 nm, which indicated that the photons with a long wavelength were more likely to be absorbed with the narrowing of the wings of the PGNB. At the near-infrared region after 985 nm, the absorption cross section kept almost constantly above $4 \times 10^4 \text{ nm}^2$, with a varied resonance wavelength dependent on wing width, and by contrast, it experienced a sharp increase in the narrow wavelength region from 885 nm to 985 nm with one order improvement of the absorption cross section area with a tiny shift of the resonance wavelength. The variation of the extinction cross section value, dependent on incident wavelength and wing width, showed a similar trend as that of the scattering cross section value, in which it increased from $4.722 \times 10^4 \text{ nm}^2$ to $1.111 \times 10^5 \text{ nm}^2$ with a blue shift from 1127 nm to 885 nm. It indicated that scattering dominated the extinction.

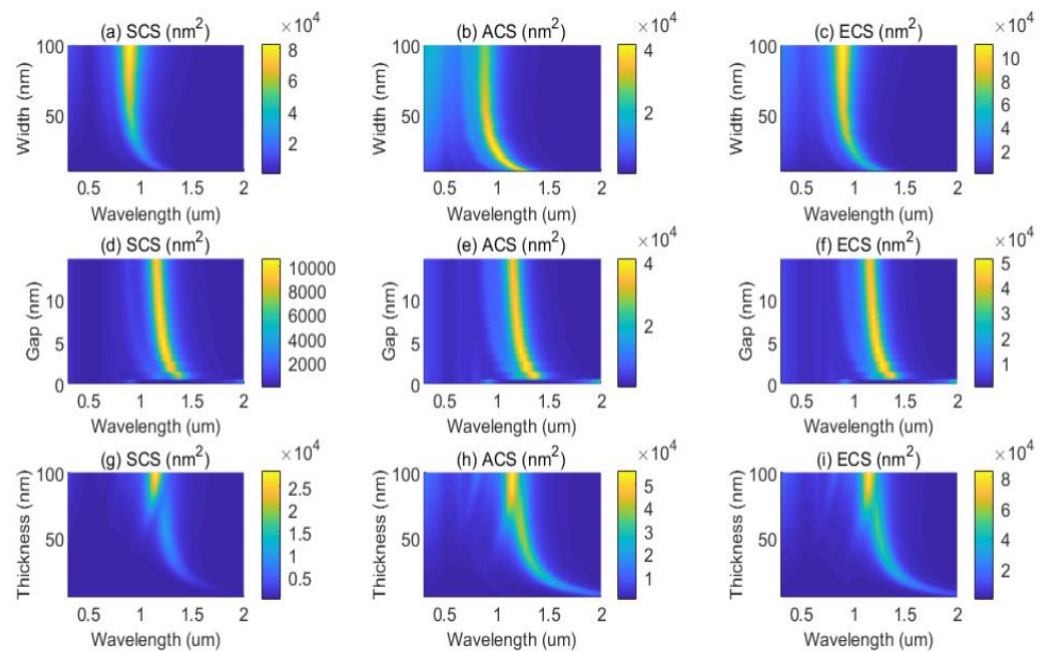


Figure 2. Scattering cross section, absorption cross section, and extinction cross section of the PGNB on a flat sapphire substrate depend on various geometrical parameters (width, gap size, and thickness of the PGNB) and the incident wavelength. The incident light source, with a wavelength range between 0.3 μm and 2 μm and a polarization angle of 90 degrees (the polarization direction was oriented at the y -axis), was illuminated on the PGNB vertically. (a–c): the scattering cross section, absorption cross section, and extinction cross section of the PGNB depend on the width of the nanobowtie and the incident wavelength; (d–f): the scattering cross section, absorption cross section, and extinction cross section of the PGNB depend on the gap size between each gold nanoparticle and the incident wavelength; (g–i): the scattering cross section, absorption cross section, and extinction cross section of the PGNB depend on the thickness of the nanobowtie and incident wavelength.

The result in Figure 2d–f shows a red shift of the resonance wavelength from 1147 nm to 1372 nm with a decrease of the gap size from 15 nm to 0.6 nm for the whole scattering cross section, absorption cross section, and extinction cross section spectrum, with a defined shape of the PGNB with a constant wing length of 100 nm, a constant wing width of 10 nm, and a constant thickness of 50 nm. Different from Figure 2a–c, due to the variation of the gap size, all three cross section values were kept almost as constants at the resonance peaks, which indicates that the gap size has little influence on the cross section values since it does not lead to any change of the surface area for the PGNB. When the gap size was reduced to 0.3 nm or 0, the two parabola-like wings almost connected with each other, and all three cross sections showed a slight decrease. The result in Figure 2g–i presents that the resonance wavelength blue-shifted from 2 μm to 1147 nm for all three cross section values while increasing the thickness from 5 nm to 100 nm, with a determined wing length of 100 nm, a wing width of 10 nm, and a gap size of 3 nm. With the increase of the thickness, the values of all three cross sections improved continuously. The maximum value of all three cross sections (scattered cross section: $2.85 \times 10^4 \text{ nm}^2$, absorption cross section: $5.58 \times 10^4 \text{ nm}^2$, extinction cross section: $8.43 \times 10^4 \text{ nm}^2$) approached the maximum thickness of the PGNB. The increased surface area of the PGNB with increased thickness value resulted in improvement of the area for the scattering cross section, absorption cross section, and extinction cross section. Interestingly, with a thickness between 70.9 nm and 82.6 nm, the resonance wavelength did not red shift to a wavelength above 1147 nm but slid to 1110 nm for the scattering cross section. Similar phenomena also happened for the absorption cross section and extinction cross section; the resonance wavelength jumped to 1110 nm with a thickness of 72.9 nm for the absorption cross section, and the resonance

wavelength jumped to 1110 nm with a thickness between 72.9 nm and 78.7 nm. A split of the resonant modes happened at a thickness between 70.9 nm and 82.6 nm.

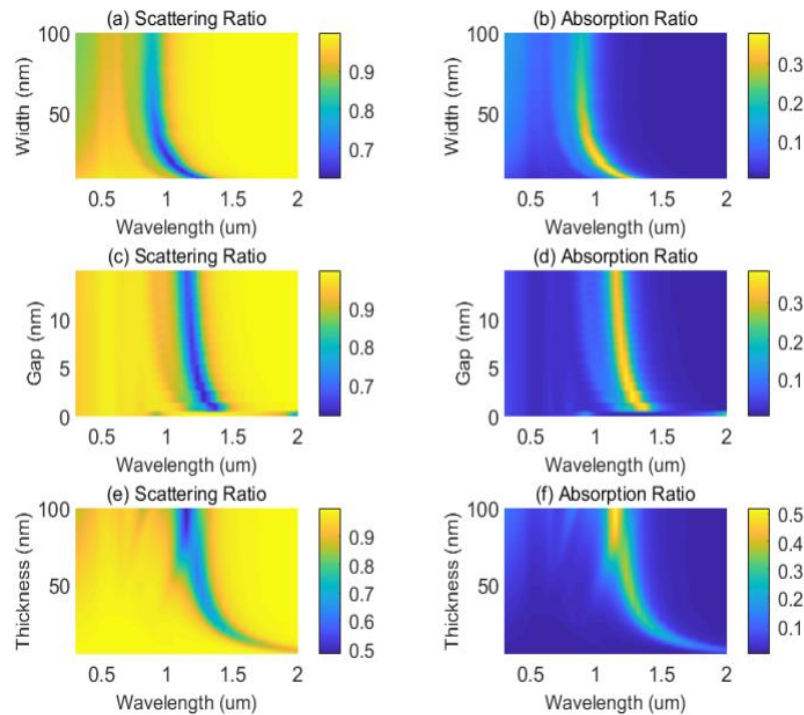


Figure 3. Scattering ratio and absorption ratio of the PGNB on a flat sapphire substrate depend on various geometrical parameters (width, gap size, and thickness of the PGNB) and incident wavelength. The incident light source, with a wavelength range between 0.3 μm and 2 μm and a polarization angle of 90 degrees (the polarization direction was oriented at the y -axis), was illuminated on the PGNB vertically. (a,b): the scattering ratio and absorption ratio of the PGNB depend on width of the nanobowtie and incident wavelength, respectively; (c,d): the scattering ratio and absorption ratio of the PGNB depend on the gap size between each gold nanoparticle and incident wavelength, respectively; (e,f): the scattering ratio and the absorption ratio of the PGNB depend on the thickness of the nanobowtie and the incident wavelength, respectively.

As presented in Figure 3, most of the photons between 300 nm and 2 μm were scattered by the PGNB, except a valley in the scattering ratio image that the value varied from 10% to 50%, and they were absorbed at the resonance peaks. As is illustrated in Figure 2, the scattering ratio and absorption ratio presented in Figure 3a,b were dependent on the variation of wing width (10–100 nm) and incident wavelength (300 nm–2 μm), with a determined wing length of 100 nm, gold thickness of 50 nm, and a gap size of 3 nm. In Figure 3a,b, with the broadening of the wing width of the PGNB, the resonance peak blue-shifted from 1227 nm to 885 nm with the absorption ratio decreasing from 35.44% (1227 nm) to 19.12% (885 nm). The maximum absorption ratio of 38.54% happened at an incident wavelength of 1186 nm with a wing width of 11.8 nm. The wavelength range where the absorption ratio was above 30% was between 908 nm and 1227 nm, with a wing width between 49 nm and 10 nm. The variation trend of the scattering ratio valley and the absorption ratio peak, dependent on incident wavelength and wing width, was the same, and the values complemented each other for conversation of energy. As well as the scattering cross section and absorption cross section described in Figure 2a–c, the scattering ratio and absorption ratio results in Figure 3a,b also uncovered the truth that a sharp vertex of the PGNB led to an increased absorption of photons with a longer wavelength. As shown in Figure 3c,d, the peak absorption ratio wavelength blue-shifted from 1372 nm to 1147 nm with an increasing of gap size from 0.6 nm to 15 nm, and the maximum absorption ratio of 38.43% happened at a gap size of 1.5 nm with an incident wavelength of 1272 nm,

a constant wing length of 100 nm, a constant wing width of 10 nm, and a gold thickness of 50 nm. Across the entire incident wavelength range (300 nm~2 μm), the absorption ratio peak varied slightly between 24.86% and 38.43%, similar to the small changes of the absorption cross section, dependent on gap size, displayed in Figure 2d–f. As illustrated in Figure 3e,f, the peak absorption ratio wavelength blue-shifted from 2 μm to 1147 nm with the increase of the thickness from 7 nm to 100 nm, while the absorption ratio value increased from 11.4% and approached its maximum at 52%, with a constant wing length of 100 nm, a constant wing width of 10 nm, and a constant gap size of 3 nm. More about the scattering and absorption property of the PGNB is reviewed in Table 1 and is also extracted from Figures 2 and 3 and presented in Figures S2–S5 in Supplementary Materials.

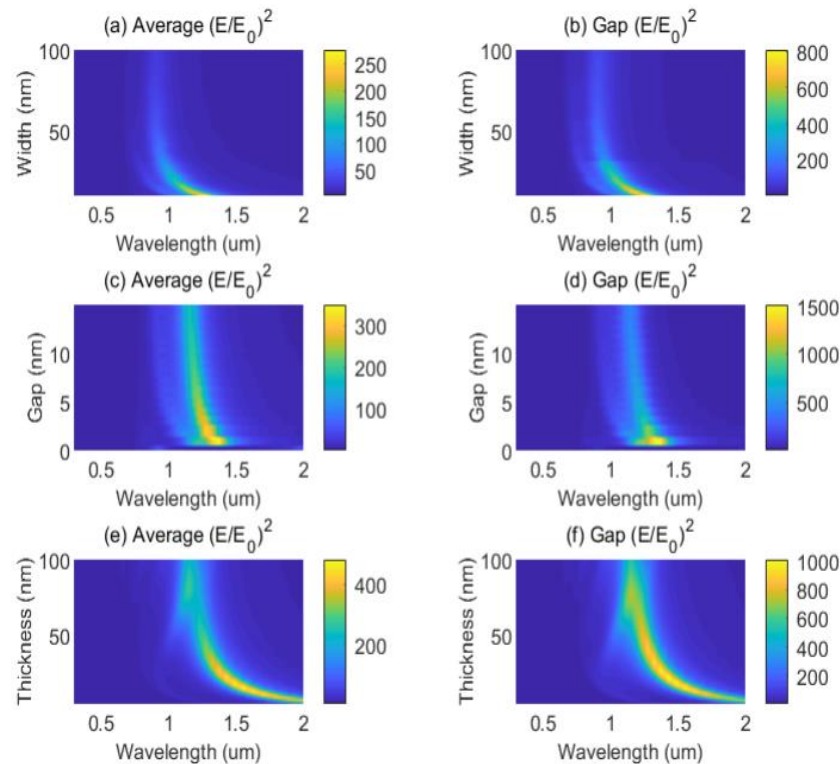


Figure 4. Average enhancement factor over the simulation object and the average enhancement factor over the gap of the PGNB on a flat sapphire substrate depend on various geometrical parameters and incident wavelength. The incident light source, with a wavelength range between 0.3 μm and 2 μm and a polarization angle of 90 degrees (the polarization direction was oriented at the y -axis), was illuminated on the PGNB vertically. (a,b): the average enhancement factor over the simulation object and the average enhancement factor over the gap of the PGNB depend on width and incident wavelength, respectively; (c,d): the average enhancement factor over the simulation object and the average enhancement factor over the gap of the PGNB depend on the gap size and incident wavelength; (e,f): the average enhancement factor over the simulation object and the average enhancement factor over the gap of the PGNB depend on the thickness and incident wavelength.

3.2. Optimization of the Field Enhancement Factor $(E/E_0)^2$

The field enhancement factor is a value that evaluates the ability of plasmonic nanostructures to confine light waves in subwavelength volumes and augment the localized field close to itself. As the field enhancement factor depends on the spatial distribution of the metallic nanostructure, the average field enhancement factor over the volume enclosing the whole simulation object and the average field enhancement factor over the gap region with a specified volume were calculated using expression (4)–(6). The simulation result regarding the average enhancement factor over the simulation object region and the enhancement factor over the gap region, dependent on various geometrical parameters, is displayed in Figure 4a–f.

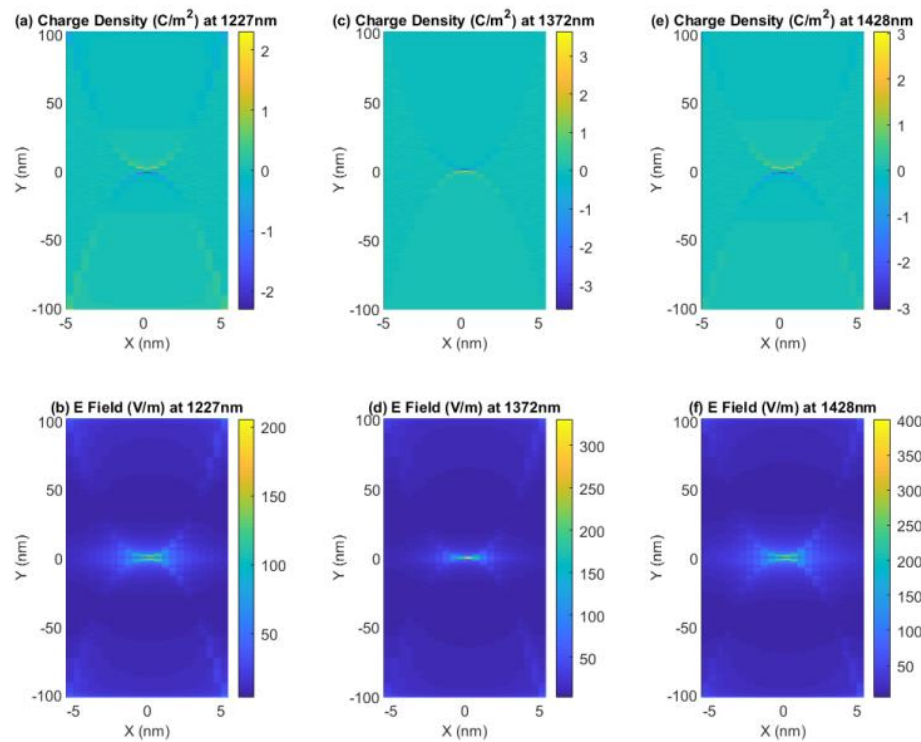


Figure 5. Charge density and electric field distribution on surface of the PGNB at the resonance wavelength with the maximum field enhancement factor at the gap corresponding to Figure 4b,d,f. (a) Charge density at resonance wavelength 1227 nm with a wing width of 10 nm; (b) Electric field distribution at resonance wavelength 1227 nm with a wing width of 10 nm; (c) Charge density at resonance wavelength 1372 nm with a gap size of 0.9 nm. (d) Electric field distribution at the resonance wavelength 1372 nm with a gap size of 0.9 nm. (e) Charge density at resonance wavelength 1428 nm with a thickness of 20.5 nm. (f) Electric field at resonance wavelength 1428 nm with a thickness of 20.5 nm.

Table 1. Scattering, absorption, extinction cross section, absorption ratio, and resonance shift depend on geometry of the PGNB on a sapphire substrate.

Wing Length 100 nm (nm)	Wing Width	Thickness	Gap Size	Wing Width	Thickness	Gap Size	Wing Width	Thickness	Gap Size
	10~100	50	3	10	50	0~15	10	5~100	3
Scattering cross section (nm ²)	Increase to 8.287×10^4 nm ² from 9.668×10^3 nm ²			Above 8.048×10^3 nm ² , slight variation			Increase to 2.847×10^4 nm ² from 360.5 nm ²		
Absorption cross section (nm ²)	Above 3.6×10^4 nm ² (>908 nm), sharp decrease to 2.8×10^4 nm ² at 885 nm			Above 3.5×10^4 nm ² , slight variation			Increase to 5.578×10^4 nm ² from 4.306×10^3 nm ²		
Extinction cross section (nm ²)	Increase to 1.1×10^5 nm ² from 4.7×10^4 nm ²			Above 4.4×10^4 nm ² , slight variation			Increase to 8.425×10^4 nm ² from 4.4×10^3 nm ²		
Absorption ratio	0.29~0.35 (>908 nm), jump to 0.19 at 885 nm			Between 0.32 and 0.38			Increase to 0.5196 from 0.04		
Resonance shift	Blue shift from 1227 nm to 886 nm			Blue shift from 2 μm to 1148 nm			Blue shift from 2 μm to 1147 nm		

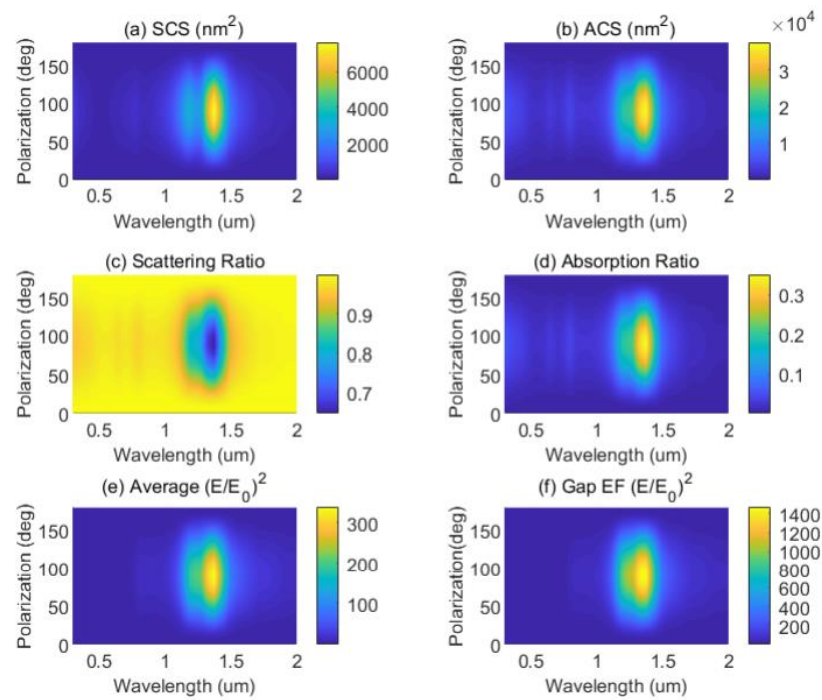


Figure 6. Scattering cross section, absorption cross section, scattering ratio, absorption ratio, average enhancement factor over the simulation object, and average enhancement factor over the gap for the PGNB on a flat sapphire substrate depend on polarization angle and incident wavelength of the source. The incident light source, with a wavelength range between 0.3 μm and 2 μm and at various polarization angle, was illuminated on the PGNB vertically. (a,b): the scattering cross section and the absorption cross section of the PGNB depend on polarization angle and wavelength of the incident light source, respectively; (c,d): the scattering ratio and the absorption ratio of the PGNB depend on polarization angle and wavelength of the incident light source, respectively; (e,f): the average enhancement factor over the simulation object and the average enhancement factor over the gap of the PGNB depend on the polarization angle and wavelength of the incident light source, respectively.

As can be seen in Figure 4a,b, with the narrowing of the wing width from 100 nm to 10 nm, the resonance peak red-shifted from 911 nm to 1274 nm, and the field average enhancement factor improved over the simulation object region from 23 to 277. Meanwhile, the resonance peak red-shifted from 911 nm to 1230 nm, and the field average enhancement factor improved over the gap region from 99 to 811. The resonance peak red-shifted significantly from 910 nm to about 1.3 μm with the narrowing of the wing width from 45 nm to 10 nm, as shown in Figure 4a,b, and the field enhancement factor continuously improved both over the simulation object and the gap region. The amount the average enhancement factor improved over the simulation object ranged from 52 (resonance peak at 910 nm) to 277 (resonance peak at 1274 nm), and meanwhile, the field enhancement factor in the gap region improved from 187 (resonance peak 911 nm) to 811 (1230 nm). However, with a larger wing width between 45 nm and 100 nm, the resonance peaks kept almost at a constant value of 911 nm without a distinguishable shift, and the average enhancement factor over the simulation object region and the gap region was under 52 and 187, respectively. Therefore, from the field enhancement factor values from two different definitions, we can see that the PGNB with sharp tips was more helpful in confining light waves in the nano-cavity and resulted in significant enhancement of the electric field, which supported previous research about the “lighting rod effect” from a view based on classical electromagnetics [49]. The charge density and the electric field distribution on the surface of the PGNB are displayed in Figure 5 at the resonance wavelength with the maximum enhancement factor in the gap region. From Figure 5a,b it can be seen that the charge density and electric field distribution presented at a resonance peak of 1227 nm (with a

wing width of 10 nm), at which the enhancement factor in the gap region approached its maximum value 811. It can be seen that most of the positive charges and negative charges were strongly confined to the two sharp tips of the PGNB, while very few charges occupied other areas of the PGNB (Figure 5a). The crowding of the charges at the two sharp tips with opposite electrical properties resulted in a significantly enhanced electric field at the gap region between the two sharp gold tips (Figure 5b).

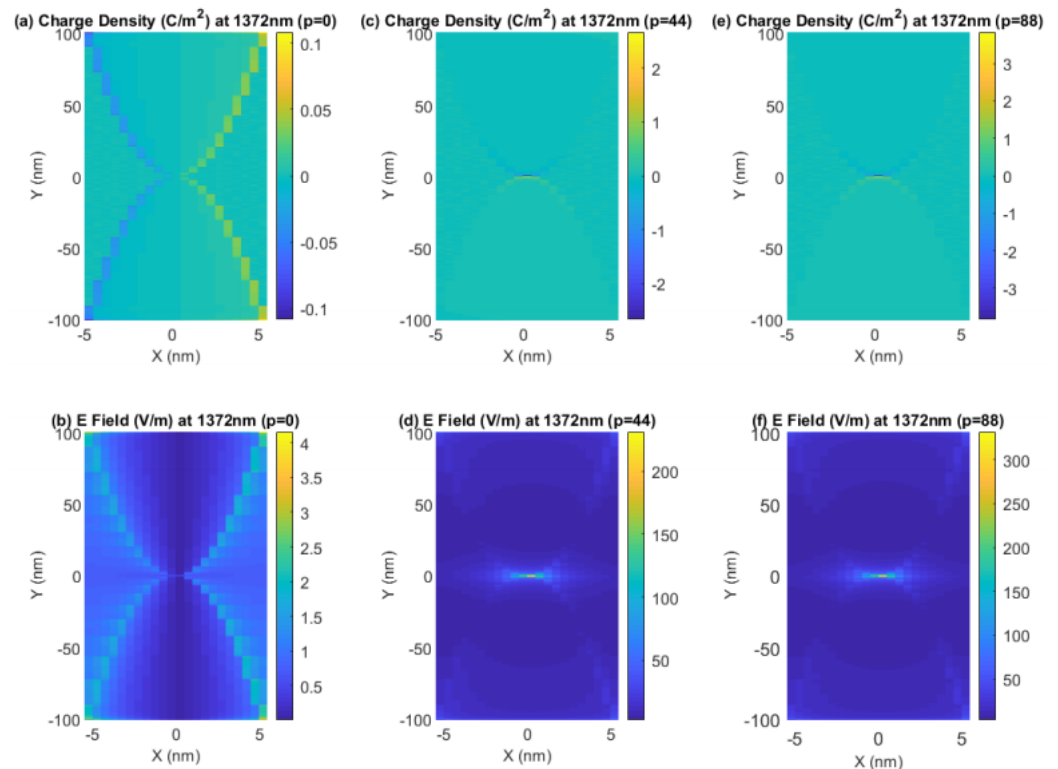


Figure 7. Charge density and electric field on surface of the PGNB illuminated under sources with different polarization angles (wing length: $L = 100$ nm, wing width: $W = 10$ nm, gold thickness: $H = 50$ nm, gap size: $\text{Gap} = 0.9$ nm). (a,b): Charge density and electric field under illumination of source with an incident wavelength of 1372 nm and a polarization angle of zero. (c,d): Charge density and electric field under illumination of source with an incident wavelength of 1372 nm and a polarization angle of 44 degrees. (e,f): Charge density and electric field under illumination of source with an incident wavelength of 1372 nm and a polarization angle of 88 degrees.

As can be seen in Figure 4c,d, with reduction of the gap size between the PGNB from 15 nm to 0.6 nm, both the resonance peaks for the average field enhancement factor over the simulation object region and the gap region experienced a red shift from 1149 nm to 1374 nm. The difference was that the resonance peaks for the average field enhancement factor over the simulation object region continued the red shift to 2 μm with a further decrease of the gap size to 0, while the average field enhancement factor over the gap region reversed the direction for a blue shift to 911 nm (both at a gap size of 0.3 nm and 0 nm). In the variation region of gap size 15 nm–0.6 nm, the average field enhancement factor over the gap region was between 428 and 1504: much higher than the value (between 177 and 352) over the simulation object region. Both the enhancement factor for the whole simulation object and for the gap region experienced significant improvement with the decreasing of the gap size. However, when the gap size was reduced to under 0.6 nm, the enhancement factor in the gap region decreased to 74 suddenly, while the resonance peak blue-shifted to 911 nm, since the two sharp tips of the PGNB connected or almost connected with each other (both with gap size of 0 and 0.3). Therefore, the field was more likely to be confined in the gap region, with the decreasing of the gap size, for a specified shape

of the PGNB with a sharp vertex. The charge density and the electric field distribution over the surface of the PGNB are displayed in Figure 5c,d, respectively, at a gap size of 0.9 nm, which approached the maximum field enhancement factor in the gap region with a resonance peak of 1372 nm. Rather significant crowding of positive and negative charges at the sharp tips of the PGNB was observed, as in Figure 5c, and it led to a significant enhancement of the electric field at the narrow gap, as shown in Figure 5d.

As can be seen from Figure 4e,f, with the thinning of the gold thickness from 100 nm to 5 nm, the resonance peaks for both the average enhancement factor over the simulation object region and the gap region experienced a red shift from 1149 nm to 2 μ m. With a gold thickness reduced from 69 nm to 5 nm, the resonance peaks experienced significant shifts between 1118 nm and 2000 nm for the enhancement factor in gap region and between 1208 nm and 2000 nm for the enhancement factor over the simulation object. By contrast, with a gold thickness reduced from 100 nm to 71 nm, the resonance peaks for both the enhancement factor in the gap region and the enhancement factor over the simulation object kept at an almost constant wavelength of 1149 nm. In contrast to the variation of wing width and gap size in which the enhancement factor experienced a monotone increase with the narrowing of the size, the field enhancement factor increased with the thinning of the gold thickness at first and started to decrease while approaching a maximum value with the continuous thinning of the gold thickness. The field enhancement factor value over the simulation object region approached its maximum 484 at a resonance wavelength of 1557 nm (gold thickness 16.6 nm), and the field enhancement factor value over the gap region touched its maximum 1019 at a resonance wavelength of 1430 nm (gold thickness 22.5 nm or 20.5 nm). The optimized gold thickness for approaching a relatively high field enhancement factor was between 7 nm and 50 nm. The charge density and electric field distribution at an optimized gold thickness of 20.5 nm and with a resonance peak of 1428 nm, at which the enhancement factor approached its maximum value, are displayed in Figure 5e,f. The significant confinement of positive charges and negative charges at the two sharp tips of the PGNB led to a strong enhancement of the electric field at the gap region and resulted in the maximum enhancement factor in the gap resonance. The tiny shift in the resonance wavelength when the enhancement factor in the gap region approached its maximum value, was seen in Figure 4b,d,f and Figure 5, was due to the interpolation error during calculating the gap enhancement factor with a redefined frequency vector owning high-denseness frequency points. More details about the average enhancement factor over the simulation object and the enhancement factor in the gap region and their relationships with geometry parameters were reviewed in Table 2 and also were extracted out of the images in Figure 4 and displayed in Figures S6–S8 in the Supplementary Materials.

3.3. Influence of the Polarization Angle for the Light Source

All the results discussed above were obtained with a vertical incidence of the light source at a polarization angle of 90 degrees where the oscillation direction of the incident electric field matched with the axis of the PGNB. The values of the scattering cross section, absorption cross section, scattering ratio, absorption ratio, average field enhancement factor over the simulation object region, and the average field enhancement factor over the gap region, dependent on the polarization angle and incident wavelength, are displayed in Figure 6, with a determined shape of the PGNB (wing length: $L = 100$ nm, wing width: $W = 10$ nm, gold thickness: $H = 50$ nm, gap size: Gap = 0.9 nm).

Table 2. Average enhancement factor, gap enhancement factor, and resonance shift depend on geometry of the PGNB on a sapphire substrate.

Wing Length 100 nm (nm)	Wing Width	Thickness	Gap Size	Wing Width	Thickness	Gap Size	Wing Width	Thickness	Gap Size	
	10~100	50	3	10	50	0~15	10	5~100	3	
Average enhancement factor	Maximum value	EFmax = 276.9 at resonance wavelength 1274 nm, with a wing width of 10 nm.			EFmax = 351.7 at resonance wavelength 1322 nm with a gap size of 1.2 nm.			EFmax = 484 at resonance wavelength 1557 nm with a thickness of 16.63 nm.		
	Variation trend	EF increased with red shift of resonance wavelength from 911 nm (EF = 52.45) to 1274 nm (EF = 276.9).			EF increased with red shift of resonance wavelength from 1149 nm (EF = 177, gap = 15 nm) to 1322 nm (EF = 351.7, gap = 1.2 nm), slightly decreased at resonance wavelength 1374 nm (EF = 346.9, gap = 0.9 nm/0.6 nm).			EF increased with red shift of resonance wavelength from 1149 nm (EF = 232.6, thickness = 100 nm) to 1157 nm (EF = 484, thickness = 16.63 nm), then decreased to EF = 420 at resonance wavelength 2 μm.		
Gap enhancement factor	Maximum value	EFmax = 811 at resonance wavelength 1230 nm, with a wing width of 10 nm.			EFmax = 1504 at resonance wavelength 1374 nm with a gap size of 0.9 nm or 0.6 nm.			EFmax = 1019 at resonance wavelength 1430 nm with a thickness of 22.45 nm.		
	Variation trend	EF increased with red shift of resonance wavelength from 910 nm (187) to 1274 nm (811).			EF increased with red shift of resonance wavelength from 911 nm (EF = 74, gap = 15 nm) to 1374 nm (EF = 1504, gap = 0.9 nm or 0.6 nm).			EF increased with red shift of resonance wavelength from 1149 nm (EF = 561, thickness = 100 nm) to 1430 nm (EF = 1019, thickness = 22.45 nm), then decreased to EF = 768.5 at resonance wavelength 2 μm.		
Resonance shift	Blue shift from about 1230 nm (wing width of 10 nm) to 911 nm (wing width of about 45 nm). From wing width 45 nm to 100 nm, the resonance wavelength kept at about 911 nm.			With narrowing of gap size from 15 nm to 0.6 nm, resonance redshift 1149 nm to 1374 nm for average EF and gap EF. When gap size was reduced to under 0.6 nm, resonance blue-shifted to 911 nm (gap EF).			Blue shift from 2 μm (thickness = 5 nm) to 1149 nm (thickness = 71 nm). With a thickness from 71 nm to 100 nm, the resonance wavelength almost kept at 1149 nm.			

From Figure 6 it can be seen that all six values presented in the color scale showed a symmetry at a polarization angle of 90 degrees, covering the whole incident wavelength from 300 nm to 2 μm. From Figure 6a it can be seen that the maximum scattering cross section value 7730 nm² happened at an incident wavelength of 1372 nm with a polarization angle of 88 degrees, and the maximum absorption cross section value 3.7742 × 10⁴ nm² happened at an incident wavelength of 1372 nm with a polarization angle of 88 degrees and 92 degrees, because 90 degrees did not appear in the discrete vector of the polarization angle (0–180 degrees). The maximum values of the scattering cross section and absorption cross section were a little bit larger than the values illustrated above in the case of the polarization angle being 90 degrees due to the symmetry of the PGNB. With deviation of the polarization angle from 90 degrees to 0 degrees or 180 degrees, the value of the scattering cross section and absorption cross section decreased quickly.

From Figure 6c,d it can be seen that the scattering ratio and the absorption ratio also showed symmetry at the polarization angle of 90 degrees, just as the scattering cross section did. The maximum absorption ratio 35.324% happened at an incident wavelength of 1372 nm and a polarization angle of 88 degrees (92 degrees). The region where the absorption ratio was above 20%, was located in a wavelength range from 1272 nm to 1428 nm and a polarization angle between 51.4 degrees and 128.6 degrees. The region where the scattering ratio value was above 80%, covered most of the incident wavelength range and polarization angle range, except the region that showed a high absorption ratio above 20%. The enhancement factor in the gap region showed a maximum value

1.46×10^3 at an incident wavelength of 1348 nm and a polarization angle of 88 degrees (92 degrees). Taking into account the other region of the PGNB, the maximum value 338 of the average enhancement factor over the simulation object became much lower than that in the gap region with a red-shifted incident wavelength of 1374 nm at the same polarization angle of 88 degrees (92 degrees). With deviation of the polarization angle from 90 degrees, both the enhancement factor in the gap region and the average enhancement factor over the simulation object decreased for the same incident wavelength, as in Figure 6e,f. The curves of the enhancement factor in the gap region, dependent on incident wavelength at various polarization angles (0, 44, 88, 121, and 151), are displayed in Figure S9 in the Supplementary Materials, presenting how the enhancement factor values between 300 nm and 2 μm reduced with the deviation of polarization angle from 90 degrees.

The images of the charge density and electric field distribution at the surface of the PGNB under the illumination of light waves at 1372 nm for various polarization angles 0, 44 degrees, and 88 degrees, are presented in Figure 7a–f, in which it is illustrated how the polarization angle influences the charge density and results in the electric field variation in the gap region. With a zero-polarization angle, most of the charges were distributed at the edge of the PGNB, and it resulted in a very low electric field in the gap region (Figure 7a,b). Reversely, the electric field at the edge of the PGNB showed a little bit higher than that in the other area. With a polarization angle of 44 degrees, some of the charges were crowded at the sharp tips of the PGNB with the opposite electric property (with a maximum value larger than 2.5 C/m^2); thus, it led to an increased electric field in the gap region with a maximum value larger than 200 V/m, as presented in Figure 7c,d. Upon further improving the polarization angle to 88 degrees (very close to the symmetric axis of 90 degrees), most of charges were confined to the two sharp tips of the PGNB (with a maximum charge density larger than 3 C/m^2); therefore, a rather strong electric field was formed in the gap region with a value larger than 300 V/m, as shown in Figure 7e,f. Matching the polarization with the middle line of the PGNB resulted in high-density charges being trapped at the two sharp tips, while the electrons in the gold material was interacted with the field from the light wave, which produced a highly enhanced electric field at the gap region.

3.4. Feasibility for Nanofabrication of the PGNB

With reference to the nanofabrication of a PGNB on a sapphire substrate, the gold thin film can normally be accurately deposited on a sapphire substrate by an e-beam evaporator with a quartz crystal monitor for thickness control or by a sputter system with a controlled deposition rate to achieve a target thickness. For good adhesion to the surface of the substrate, a thin titanium film within 5 nm is usually deposited in advance of the gold thin film. The PGNB with a size on the subwavelength scale, especially with a tiny gap size of less than 10 nm, presents a big challenge for conventional photolithography methods to transfer the pattern due to the Abbe diffraction limit. However, special nanofabrication facilities, such as extreme ultraviolet multibeam interference lithography (EUV-IL), electron beam lithography (EBL) technology, direct laser writing lithography (DLW), focused ion beam miller (FIB), and electron beam miller (EBM) make the nanofabrication available to some extent [50–52]. The EUV-IL was reported to fabricate high quality gratings with periodicities down to 14 nm [50]. Combined with a glancing angle thermal evaporation, sub-10-nm gaps between Cr strips on a hydrogen silsesquioxane (HSQ) line array were fabricated by evaporating with a rotation of the substrate [53]. Taking advantage of a short de Broglie wavelength of high-energy electrons, the electron beam was focused on a rather small spot size of 1 nm with a large focus depth of several microns [50]. With negative HSQ resistance, a gap size as small as 5 nm between two gold disks was reported to be fabricated [54]. Taking advantage of the phenomenon where a tiny extension of the CrOx film happens when a Cr mask is oxidized, a small gap with a size of 3 nm between two gold squares (100 nm \times 80 nm) was fabricated by a nanofabrication process of electron beam lithography combined with lift-off and wet etching [55]. With 405 nm DLW lithography, a gap width as small as 5 nm in an array was achieved by optimization of the laser beam

intensity and scanning rate [56]. The reported works, based on lithography techniques, such as EUV-IL, EBL, and DLW, announced that these technologies had the feasibility to fabricate a PGNB on a sapphire substrate with a gap size within 10 nm. Aside from lithography methods, FIB is a technique that can mill the material with the focus of a gallium ion beam (GIB) or helium ion beam (HIB) on the surface of a substrate [51]. With a combination of coarse milling by a GIB and fine milling by a HIB, a triangle-shaped gold nanobowtie with a gap of less than 6 nm was reported [57]. In the case where the EBM was used to fabricate the fine features of a nanobowtie, a rather small nanogap within 2 nm was reported to be possible on a platinum film [58]. Other methods, such as the electromigration technique, which uses a current flowing through a notch on a narrow strip of pre-patterned metallic thin film to cause necking and splitting, were reported to be able to fabricate a nanogap on a gold electrode with a size less than 2 nm [59]. For nanofabrication of the PGNB in this article, a milling method combined with HIB for coarse formation of each wing and EBM for precisely making the tiny nanogap can be used. Taking advantage of the electromigration technique to manufacture the nanogap on a predefined PGNB with a narrow strip connected each wing is another choice.

4. Conclusions

In summary, the light scattering, absorption, and field enhancement of the PGNB were strongly dependent on its geometry such as the wing length, wing width, and gold thickness. According to the calculation above, the resonance wavelength experienced a red shift from 900 nm to 1.2 μm , approximately, with the narrowing of the wing width from 100 nm to 10 nm (wing length: 100 nm, thickness: 50 nm, and gap size: 3 nm). The scattering cross section and extinction cross section of the PGNB continuously increased with the widening of the wing width until they approached their maximums. By contrast, the absorption cross section decreased slightly with the broadening of the wing width and the corresponding blue shift of the resonance wavelength. There existed an optimized wing width from 10 nm to 49 nm with a corresponding resonance wavelength from 1227 nm to 908 nm that made the absorption ratio larger than 30%. Meanwhile, the field enhancement at the gap region between the two parabola-like wings improved by more than 8 times with the narrowing of the wing width due to more charges being trapped in the tip-to-tip-type sharp gold tips. With reduction of the gap size between the two gold tips, the nano-cavity experienced a red shift for the resonance wavelength from 1147 nm to 1372 nm without significant variation of the scattering cross section and absorption cross section (wing length: 100 nm, wing width: 10 nm, thickness: 50 nm). However, the field enhancement factor in the gap region was quite sensible to the gap size, which it improved continuously from 428 to 1504 with the reduction of the gap size from 15 nm to 0.6 nm, excluding the connection of the two gold tips. The resonance wavelength of the nano-cavity blue-shifted between 2 μm and 1147 nm, approximately, with the increasing of the gold thickness from 5 nm to 100 nm, accompanied by continuous improvement of the scattering cross section and absorption cross section (wing length: 100 nm, wing width: 10 nm, gap size: 3 nm). The field enhancement factor in the gap region started to improve with the increasing of the gold thickness until it reached a maximum value of 1019 at a thickness of 20.51 nm (22.45 nm). A thickness window between 7 nm and 50 nm existed for a high field enhancement factor above 768.5. Further research on the polarization angle of the incident source pointed out that aligning the electric field direction of the incident light with the axis of the PGNB ensured a larger scattering cross section, a larger absorption cross section, a bigger absorption ratio, and a higher enhancement factor in the gap region. The charge distribution on the surface of the PGNB and the field in the gap region for various polarization angles explained the physics for approaching a high field enhancement factor in the gap region. At last, the feasibility of fabricating the PGNB simulated in this article was analyzed in relation to possible modern nanofabrication techniques.

Supplementary Materials: The following supporting information can be downloaded at: <https://www.mdpi.com/article/10.3390/photonics9030193/s1>. Fitting of the n k values of gold and sapphire used in this simulation with physical models is displayed in Figure S1. The values of the scattering cross section, absorption cross section, and extinction cross section dependent on resonance wavelength with variation of each geometry parameter and the relationship between various geometry parameters and the resonance wavelength are displayed in Figures S2–S4. The absorption ratio, dependent on resonance wavelength according to the variation of wing width, gap size, thickness, and also the relationship between the geometry parameters and the resonance wavelength, are displayed in Figure S5. The average field enhancement factor over the simulation object (the field enhancement factor in the gap region), dependent on resonance wavelength according to the variation of wing width, gap size, thickness, and also the relationship between the geometry parameters and the resonance wavelength, are displayed in Figures S6–S8. The enhancement factor in the gap region depends on incident wavelength at various polarization angle is displayed in Figure S9.

Author Contributions: Conceptualization, W.L.; methodology, W.L.; formal analysis, J.Z. and X.T.; data curation, Z.Y.; software, B.L.; resources, B.L.; supervision, B.L.; writing—original draft, W.L.; writing—review & editing, C.P.C. and Y.Z.; funding acquisition, C.P.C. All authors have read and agreed to the published version of the manuscript.

Funding: The research is funded by National Natural Science Foundation of China (61901264, 61831015), Science and Technology Commission of Shanghai Municipality (19ZR1427200), and Natural Science Foundation of Chongqing, China (cstc2021jcyj-msxmX1136).

Institutional Review Board Statement: Not applicable.

Informed Consent Statement: Not applicable.

Data Availability Statement: Data is presented in the main text of this article and the supplementary materials.

Acknowledgments: The authors appreciate the reviewers taking time to read this manuscript and to give helpful suggestions for further improvement.

Conflicts of Interest: The authors declare no conflict of interest.

References

1. Baumberg, J.J.; Aizpurua, J.; Mikkelsen, M.H.; Smith, D.R. Extreme nanophotonics from ultrathin metallic gaps. *Nat. Mater.* **2019**, *18*, 668–678. [[CrossRef](#)]
2. Ciraci, C.; Hill, R.T.; Mock, J.J.; Urzhumov, Y.; Fernández-Domínguez, A.I.; Maier, S.A.; Pendry, J.B.; Chilkoti, A.; Smith, D.R. Probing the Ultimate Limits of Plasmonic Enhancement. *Science* **2012**, *337*, 1072–1074. [[CrossRef](#)]
3. Li, W.; Tong, X.; Yang, Z.; Zhang, J.; Liu, B.; Chen, C.P. Improved Sensitivity of Surface-Enhanced Raman Scattering with Gold Nanoparticles-Insulator-Metal Sandwich Layers on Flat Sapphire Substrate. *Nanomaterials* **2021**, *11*, 2416. [[CrossRef](#)] [[PubMed](#)]
4. Jain, P.K.; Huang, W.; El-Sayed, M.A. On the Universal Scaling Behavior of the Distance Decay of Plasmon Coupling in Metal Nanoparticle Pairs: A Plasmon Ruler Equation. *Nano Lett.* **2007**, *7*, 2080–2088. [[CrossRef](#)]
5. Li, W. Physics Models of Plasmonics: Single Nanoparticle, Complex Single Nanoparticle, Nanodimer, and Single Nanoparticle over Metallic Thin Film. *Plasmonics* **2018**, *13*, 997–1014. [[CrossRef](#)] [[PubMed](#)]
6. Christiansen, R.E.; Michon, J.; Benzaouia, M.; Sigmund, O.; Johnson, S.G. Inverse design of nanoparticles for enhanced Raman scattering. *Opt. Express* **2020**, *28*, 4444–4462. [[CrossRef](#)] [[PubMed](#)]
7. Crozier, K.B.; Zhu, W.; Wang, D.; Lin, S.; Best, M.D.; Camden, J.P. Plasmonics for Surface Enhanced Raman Scattering: Nanoantennas for Single Molecules. *IEEE J. Sel. Top. Quantum Electron.* **2014**, *20*, 152–162. [[CrossRef](#)]
8. Li, W.; Zhao, X.; Yi, Z.; Glushenkov, A.M.; Kong, L. Plasmonic substrates for surface enhanced Raman scattering. *Anal. Chim. Acta* **2017**, *984*, 19–41. [[CrossRef](#)] [[PubMed](#)]
9. Ma, L.; Yu, P.; Wang, W.; Kuo, H.-C.; Govorov, A.O.; Sun, S.; Wang, Z. Nanoantenna-Enhanced Light-Emitting Diodes: Fundamental and Recent Progress. *Laser Photonics Rev.* **2021**, *15*, 2000367. [[CrossRef](#)]
10. Wang, H.; Guo, Y.; Hao, H.; Bian, H.; Aubin, H.; Wei, Y.; Li, H.; Liu, T.; Degiron, A.; Wang, H. Bright CdSe/CdS Quantum Dot Light-Emitting Diodes with Modulated Carrier Dynamics via the Local Kirchhoff Law. *ACS Appl. Mater. Interfaces* **2021**, *13*, 56476–56484. [[CrossRef](#)] [[PubMed](#)]
11. Cheng, X.; Rodriguez, M.; Wang, Y. Native fluorescence enhancement using an Aluminum bowtie nano-antenna. *SPIE* **2020**, *11466*, 10–14.

12. Salah, O.; Fahmy, A.N.F.; Farhat, O.H.M.; Hussein, A.M. Optical Nano-Antennas for Energy Harvesting. In *Information Resources Management, Renewable and Alternative Energy: Concepts, Methodologies, Tools, and Applications*; IGI Global: Hershey, PA, USA, 2017; pp. 161–196.
13. Castilla, S.; Vangelidis, I.; Pusapati, V.-V.; Goldstein, J.; Autore, M.; Slipchenko, T.; Rajendran, K.; Kim, S.; Watanabe, K.; Taniguchi, T.; et al. Plasmonic antenna coupling to hyperbolic phonon-polaritons for sensitive and fast mid-infrared photodetection with graphene. *Nat. Commun.* **2020**, *11*, 4872. [[CrossRef](#)] [[PubMed](#)]
14. Chen, B.; Ji, Z.; Zhou, J.; Yu, Y.; Dai, X.; Lan, M.; Bu, Y.; Zhu, T.; Li, Z.; Hao, J.; et al. Highly polarization-sensitive far infrared detector based on an optical antenna integrated aligned carbon nanotube film. *Nanoscale* **2020**, *12*, 11808–11817. [[CrossRef](#)] [[PubMed](#)]
15. He, Z.; Zhang, G.; Zhang, S.; Feng, X.; Liu, Z.; Wang, G.; Yang, S.; Ding, G. Resonant nanocavity-enhanced graphene photodetectors on reflecting silicon-on-insulator wafers. *Appl. Phys. Lett.* **2021**, *119*, 232104. [[CrossRef](#)]
16. Seitz, L.; Laible, F.; Dickreuter, S.; Gollmer, D.A.; Kern, D.P.; Fleischer, M. Miniaturized fractal optical nanoantennas defined by focused helium ion beam milling. *Nanotechnology* **2019**, *31*, 075301. [[CrossRef](#)]
17. Horák, M.; Bukvišová, K.; Švarc, V.; Jaskowicz, J.; Krápek, V.; Šikola, T. Comparative study of plasmonic antennas fabricated by electron beam and focused ion beam lithography. *Sci. Rep.* **2018**, *8*, 9640. [[CrossRef](#)] [[PubMed](#)]
18. Liu, B.; Zhan, C.; Yao, X.; Yan, S.; Ren, B. Nanobowtie arrays with tunable materials and geometries fabricated by holographic lithography. *Nanoscale* **2020**, *12*, 21401–21408. [[CrossRef](#)] [[PubMed](#)]
19. Krápek, V.; Konečná, A.; Horák, M.; Ligmajer, F.; Stöger-Pollach, M.; Hrtoň, M.; Babocký, J.; Šikola, T. Independent engineering of individual plasmon modes in plasmonic dimers with conductive and capacitive coupling. *Nanophotonics* **2020**, *9*, 623–632. [[CrossRef](#)]
20. Guo, R.; Kinzel, E.C.; Li, Y.; Uppuluri, S.M.; Raman, A.; Xu, X. Three-dimensional mapping of optical near field of a nanoscale bowtie antenna. *Opt. Express* **2010**, *18*, 4961–4971. [[CrossRef](#)] [[PubMed](#)]
21. Kaniber, M.; Schraml, K.; Regler, A.; Bartl, J.; Glashagen, G.; Flassig, F.; Wierzbowski, J.; Finley, J.J. Surface plasmon resonance spectroscopy of single bowtie nano-antennas using a differential reflectivity method. *Sci. Rep.* **2016**, *6*, 23203. [[CrossRef](#)] [[PubMed](#)]
22. Morshed, M.; Li, Z.; Olbricht, B.C.; Fu, L.; Haque, A.; Li, L.; Rifat, A.A.; Rahmani, M.; Miroshnichenko, A.E.; Hattori, H.T. High Fluence Chromium and Tungsten Bowtie Nano-antennas. *Sci. Rep.* **2019**, *9*, 13023. [[CrossRef](#)] [[PubMed](#)]
23. Huang, I.-C.; Holzgrafe, J.; Jensen, R.A.; Choy, J.T.; Bawendi, M.G.; Lončar, M. 10 nm gap bowtie plasmonic apertures fabricated by modified lift-off process. *Appl. Phys. Lett.* **2016**, *109*, 133105. [[CrossRef](#)]
24. Wang, W.; Christensen, T.; Jauho, A.-P.; Thygesen, K.S.; Wubs, M.; Mortensen, N.A. Plasmonic eigenmodes in individual and bow-tie graphene nanotriangles. *Sci. Rep.* **2015**, *5*, 9535. [[CrossRef](#)] [[PubMed](#)]
25. Du, G.; Lu, Y.; Lankanath, D.; Hou, X.; Chen, F. Theoretical Study on Symmetry-Broken Plasmonic Optical Tweezers for Heterogeneous Noble-Metal-Based Nano-Bowtie Antennas. *Nanomaterials* **2021**, *11*, 759. [[CrossRef](#)] [[PubMed](#)]
26. Wang, B.; Singh, S.C.; Lu, H.; Guo, C. Design of Aluminum Bowtie Nanoantenna Array with Geometrical Control to Tune LSPR from UV to Near-IR for Optical Sensing. *Plasmonics* **2020**, *15*, 609–621. [[CrossRef](#)]
27. Ding, W.; Bachelot, R.; Kostcheev, S.; Royer, P.; Lamaestre, R.E.D. Surface plasmon resonances in silver Bowtie nanoantennas with varied bow angles. *J. Appl. Phys.* **2010**, *108*, 124314. [[CrossRef](#)]
28. Hrtoň, M.; Konečná, A.; Horák, M.; Šikola, T.; Krápek, V. Plasmonic Antennas with Electric, Magnetic, and Electromagnetic Hot Spots Based on Babinet's Principle. *Phys. Rev. Appl.* **2020**, *13*, 054045. [[CrossRef](#)]
29. Myroshnichenko, V.; Rodríguez-Fernández, J.; Pastoriza-Santos, I.; Funston, A.M.; Novo, C.; Mulvaney, P.; Liz-Marzán, L.M.; de Abajo, F.J.G. Modelling the optical response of gold nanoparticles. *Chem. Soc. Rev.* **2008**, *37*, 1792–1805. [[CrossRef](#)] [[PubMed](#)]
30. Ding, W.; Bachelot, R.; de Lamaestre, R.E.; Macias, D.; Baudrion, A.L.; Royer, P. Understanding near/far-field engineering of optical dimer antennas through geometry modification. *Opt. Express* **2009**, *17*, 21228–21239. [[CrossRef](#)] [[PubMed](#)]
31. Benz, F.; de Nijs, B.; Tserkezis, C.; Chikkaraddy, R.; Sigle, D.O.; Pukenas, L.; Evans, S.D.; Aizpurua, J.; Baumberg, J.J. Generalized circuit model for coupled plasmonic systems. *Opt. Express* **2015**, *23*, 33255–33269. [[CrossRef](#)] [[PubMed](#)]
32. Campione, S.; Warne, L.K.; Goldflam, M.D.; Peters, D.W.; Sinclair, M.B. Improved quantitative circuit model of realistic patch-based nanoantenna-enabled detectors. *J. Opt. Soc. Am. B* **2018**, *35*, 2144–2152. [[CrossRef](#)]
33. Engheta, N. Circuits with light at nanoscales: Optical nanocircuits inspired by metamaterials. *Science* **2007**, *317*, 1698–1702. [[CrossRef](#)] [[PubMed](#)]
34. Engheta, N.; Salandrino, A.; Alù, A. Circuit Elements at Optical Frequencies: Nanoinductors, Nanocapacitors, and Nanoresistors. *Phys. Rev. Lett.* **2005**, *95*, 095504. [[CrossRef](#)] [[PubMed](#)]
35. Venediktov, V.Y.; Efremova, E.A.; Krylov, I.R.; Prokhorova, U.V. Analysis of the use of the LCR circuit model for evaluating the resonant response of thin rectangular nanoantennas. *Quantum Electron.* **2019**, *49*, 676–682. [[CrossRef](#)]
36. Hughes, T.W.; Fan, S. Plasmonic Circuit Theory for Multiresonant Light Funneling to a Single Spatial Hot Spot. *Nano Lett.* **2016**, *16*, 5764–5769. [[CrossRef](#)] [[PubMed](#)]
37. Pae, J.-S.; Im, S.-J.; Song, K.-S.; Ri, C.-S.; Ho, K.-S.; Han, Y.-H.; Herrmann, J. Deep subwavelength flow-resonant modes in a waveguide-coupled plasmonic nanocavity. *Phys. Rev. B* **2020**, *101*, 245420. [[CrossRef](#)]
38. Dudek, M.; Kowrdziej, R.; Pianelli, A.; Parka, J. Graphene-based tunable hyperbolic microcavity. *Sci. Rep.* **2021**, *11*, 74. [[CrossRef](#)] [[PubMed](#)]
39. Sullivan, D. *Electromagnetic Simulation Using the FDTD Method*; IEEE Inc.: New York, NY, USA, 2000.

40. Ciesielski, A.; Skowronski, L.; Trzcinski, M.; Górecka, E.; Trautman, P.; Szoplik, T. Evidence of germanium segregation in gold thin films. *Surf. Sci.* **2018**, *674*, 73–78. [[CrossRef](#)]
41. Palik, E.D. *Handbook of Optical Constants of Solids*; Academic Press: Pittsburgh, MD, USA, 1997.
42. Maier, S. *Plasmonics: Fundamentals and Applications*; Springer + Business Media LLC: New York, NY, USA, 2007.
43. Derkachova, A.; Kolwas, K.; Demchenko, I. Dielectric Function for Gold in Plasmonics Applications: Size Dependence of Plasmon Resonance Frequencies and Damping Rates for Nanospheres. *Plasmonics* **2016**, *11*, 941–951. [[CrossRef](#)]
44. Kheirandish, A.; Javan, N.S.; Mohammadzadeh, H. Modified Drude model for small gold nanoparticles surface plasmon resonance based on the role of classical confinement. *Sci. Rep.* **2020**, *10*, 6517. [[CrossRef](#)] [[PubMed](#)]
45. Hao, F.; Nordlander, P. Efficient dielectric function for FDTD simulation of the optical properties of silver and gold nanoparticles. *Chem. Phys. Lett.* **2007**, *446*, 115–118. [[CrossRef](#)]
46. Berenger, J.-P. A perfectly matched layer for the absorption of electromagnetic waves. *J. Comput. Phys.* **1994**, *114*, 185–200. [[CrossRef](#)]
47. Marshall, U.I.A.R. *Chapter 7 Introduction of Sources, Numerical Electromagnetics: The FDTD Method*; Cambridge University Press: Cambridge, UK, 2011.
48. Giannini, V.; Fernández-Domínguez, A.I.; Heck, S.C.; Maier, S.A. Plasmonic nanoantennas: Fundamentals and their use in controlling the radiative properties of nanoemitters. *Chem. Rev.* **2011**, *111*, 3888–3912. [[CrossRef](#)]
49. Urbietta, M.; Barbry, M.; Zhang, Y.; Koval, P.; Sánchez-Portal, D.; Zabala, N.; Aizpurua, J. Atomic-Scale Lightning Rod Effect in Plasmonic Picocavities: A Classical View to a Quantum Effect. *ACS Nano* **2018**, *12*, 585–595. [[CrossRef](#)]
50. Luo, S.; Hoff, B.H.; Maier, S.A.; de Mello, J.C. Scalable Fabrication of Metallic Nanogaps at the Sub-10 nm Level. *Adv. Sci.* **2021**, *8*, 2102756. [[CrossRef](#)]
51. He, S.; Tian, R.; Wu, W.; Li, W.-D.; Wang, D. Helium-ion-beam nanofabrication: Extreme processes and applications. *Int. J. Extrem. Manuf.* **2021**, *3*, 012001. [[CrossRef](#)]
52. Chen, Y.; Shu, Z.; Zhang, S.; Zeng, P.; Liang, H.; Zheng, M.; Duan, H. Sub-10 nm fabrication: Methods and applications. *Int. J. Extrem. Manuf.* **2021**, *3*, 032002. [[CrossRef](#)]
53. Siegfried, T.; Ekinici, Y.; Martin, O.J.; Sigg, H. Gap plasmons and near-field enhancement in closely packed sub-10 nm gap resonators. *Nano Lett.* **2013**, *13*, 5449–5453. [[CrossRef](#)]
54. Duan, H.; Hu, H.; Kumar, K.; Shen, Z.; Yang, J.K.W. Direct and Reliable Patterning of Plasmonic Nanostructures with Sub-10-nm Gaps. *ACS Nano* **2011**, *5*, 7593–7600. [[CrossRef](#)] [[PubMed](#)]
55. Zhu, W.; Banaee, M.G.; Wang, D.; Chu, Y.; Crozier, K.B. Lithographically fabricated optical antennas with gaps well below 10 nm. *Small* **2011**, *7*, 1761–1766. [[CrossRef](#)]
56. Wang, L.; Wang, C.; Zhang, H.; Xia, F.; Wang, C.; Yang, F.; Zhang, X.; Liu, Q. Fabrication-resolution enhancement method based on low-energy multiple exposures. *Opt. Express* **2015**, *23*, 29353–29359. [[CrossRef](#)]
57. Kollmann, H.; Piao, X.; Esmann, M.; Becker, S.F.; Hou, D.; Huynh, C.; Kautschor, L.-O.; Bösker, G.; Vieker, H.; Beyer, A.; et al. Toward Plasmonics with Nanometer Precision: Nonlinear Optics of Helium-Ion Milled Gold Nanoantennas. *Nano Lett.* **2014**, *14*, 4778–4784. [[CrossRef](#)]
58. Fischbein, M.D.; Drndić, M. Sub-10 nm Device Fabrication in a Transmission Electron Microscope. *Nano Lett.* **2007**, *7*, 1329–1337. [[CrossRef](#)] [[PubMed](#)]
59. Park, J.; Pasupathy, A.N.; Goldsmith, J.I.; Chang, C.; Yaish, Y.; Petta, J.R.; Rinkoski, M.; Sethna, J.P.; Abruña, H.D.; McEuen, P.L.; et al. Coulomb blockade and the Kondo effect in single-atom transistors. *Nature* **2002**, *417*, 722–725. [[CrossRef](#)] [[PubMed](#)]